Version of Record at:
https://doi.org/10.1063/5.0245736

Journal of Applied Physics

RESEARCH ARTICLE | APRIL 08 2025

Short-range order and longer-range disorder revealed in germanium–tin alloy thin films by extended x-ray absorption fine structure analysis

J. Zachary Lentz ; Haochen Zhao ; J. C. Woicik ; Yuping Zeng ; Paul C. McIntyre

Check for updates

J. Appl. Phys. 137, 145701 (2025)
https://doi.org/10.1063/5.0245736

CHORUS

View Online Export Citation

Articles You May Be Interested In

Local ordering in Ge/Ge–Sn semiconductor alloy core/shell nanowires revealed by extended x-ray absorption fine structure (EXAFS)

Appl. Phys. Lett. (February 2023)

Remote plasma-enhanced chemical vapor deposition of GeSn on Si (100), Si (111), sapphire, and fused silica substrates

J. Vac. Sci. Technol. B (August 2024)

Transferable GeSn ribbon photodetectors for high-speed short-wave infrared photonic applications

J. Vac. Sci. Technol. B (June 2024)

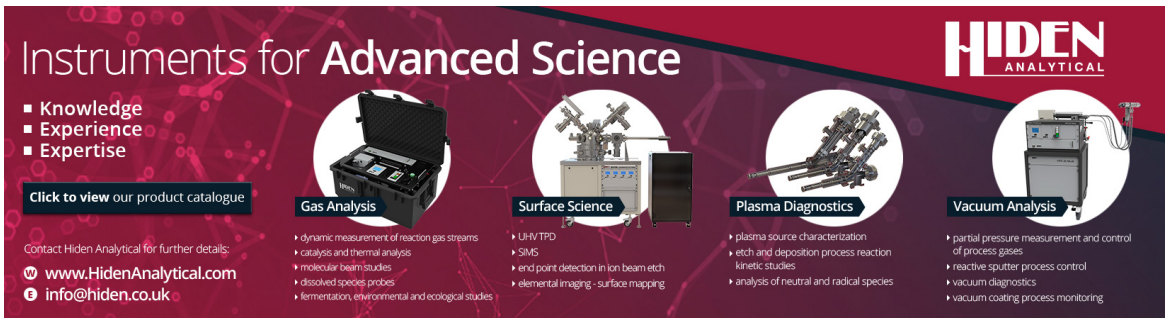

AIP Publishing

Version of Record at:
https://doi.org/10.1063/5.0245736

Journal of Applied Physics ARTICLE pubs.aip.org/aip/jap

Short-range order and longer-range disorder revealed in germanium–tin alloy thin films by extended x-ray absorption fine structure analysis

Cite as: J. Appl. Phys. **137**, 145701 (2025); doi: 10.1063/5.0245736
Submitted: 28 October 2024 · Accepted: 28 January 2025 ·
Published Online: 8 April 2025

View Online Export Citation CrossMark

J. Zachary Lentz,[1] Haochen Zhao,[2] J. C. Woicik,[3] Yuping Zeng,[2] and Paul C. McIntyre[1,4,a)]

AFFILIATIONS

[1]Department of Materials Science and Engineering, Stanford University, Stanford, California 94305, USA
[2]Department of Electrical and Computer Engineering, University of Delaware, Newark, Delaware 19716, USA
[3]Materials Measurement Science Division, Material Measurement Laboratory, National Institute of Standards and Technology, Gaithersburg, Maryland 20899, USA
[4]Stanford Synchrotron Radiation Lightsource (SSRL), SLAC National Accelerator Laboratory, Menlo Park, California 94025, USA

[a)]**Author to whom correspondence should be addressed:** pcm1@slac.stanford.edu

ABSTRACT

Short-range order (SRO) in semiconductor alloys, a relatively under-studied structural phenomenon in which local atomic arrangements differ from those of a random solid solution, is investigated in molecular beam epitaxy (MBE)-grown GeSn thin films. A novel preparation technique is used to pattern these films into microscale ribbons that are released from the substrate for extended x-ray absorption fine structure (EXAFS) analysis. The results indicate a strong SRO in which the first shell around Sn atoms is greatly denuded of Sn atoms relative to the nominal atomic composition of the alloy. This effect is more pronounced than that observed recently in GeSn nanowires grown by chemical vapor deposition. Additionally, the presence of a longer-range disorder detected by EXAFS analysis in the shells of atoms more distant from the absorbers is indicative of the defects and inhomogeneous strain present in the MBE-grown films. The evident existence of the SRO in GeSn alloys deposited by different growth methods and in different strain states suggests that SRO is a general phenomenon in the thin films of this metastable solid solution.

© 2025 Author(s). All article content, except where otherwise noted, is licensed under a Creative Commons Attribution (CC BY) license (https://creativecommons.org/licenses/by/4.0/). https://doi.org/10.1063/5.0245736

INTRODUCTION

Compositional short-range order (SRO) in the Ge–Sn alloy system (GeSn), wherein Sn atoms repel each other and, therefore, have a decreased tendency to be the first nearest neighbors (1NN), has been predicted to occur and to strongly affect the bandgap of the material.[1] This possibility is of considerable practical interest because, for sufficiently large Sn composition, GeSn has the rare characteristic of achieving a direct bandgap in an all-group-IV semiconductor system. A recent study using machine learning potentials to investigate relatively large simulation cells has further predicted that multiple types of SRO in GeSn are possible.[2] Similarly, in the ternary Si–Ge–Sn system (SiGeSn), two distinct types of SRO can occur with differing effects on the predicted semiconductor bandgap and on whether a direct or indirect transition is promoted by the ordering.[3] In this system, it has also been predicted that differing local distributions of these SRO types can yield the same average short-range order parameter but produce significantly different semiconducting properties.[4]

These interesting theoretical predictions have prompted a growing number of reports in the literature on the presence of SRO in GeSn and SiGeSn. Investigation continues concerning what may contribute to its presence or absence, in particular, materials studied depending on specifics of the alloy synthesis method/conditions and the characterization methods used. Early attempts at measuring the short-range order in GeSn were performed using atom probe tomography (APT) and the related reports found no evidence of SRO in the material.[5,6] More recent APT measurements focusing on the details of APT data analysis, especially as it concerns the detection of SRO, showed evidence of limited SRO.[7] In a previous work,[8] high-quality extended x-ray absorption fine structure (EXAFS) spectroscopy measurements of Ge core/GeSn shell

© Author(s) 2025

Version of Record at:
https://doi.org/10.1063/5.0245736

nanowires (NW) sample showed strong SRO in GeSn single crystal shells deposited around Ge core nanowires. Tin atoms in the shells were ~40% less likely to be the first nearest neighbors (1NN) of other Sn atoms compared to a random alloy, a behavior similar to that predicted by simulations. EXAFS is well-suited to the task of measuring this SRO phenomenon, given that it is the most sensitive to the closest neighbors of the absorbing atom, i.e., the 1NN shell. However, growing GeSn around Ge nanowires produces unique samples, in that, because the misfitting core nanowires act as compliant substrates, and the GeSn shells can grow essentially strain-free above a certain shell thickness.[9,10] This differs from the situation typical of planar thin film epitaxy on a bulk misfitting substrate during which residual strains often persist in the epitaxial layer even when it is grown on a buffer layer, and in which dislocations propagate from the buffer layer into the epilayer. In the present study, molecular beam epitaxy (MBE)-grown GeSn thin films deposited in the conventional planar geometry on misfitting (100) substrates were investigated with EXAFS analysis and the results were compared to those obtained from the Ge core/GeSn shell nanowires.

EXPERIMENTAL PROCEDURES

The nanowire sample was grown, as reported previously,[8] in a chemical vapor deposition (CVD) reactor, wherein the Ge core was deposited by the vapor–liquid–solid (VLS) mechanism using GeH_4(g), and the additional introduction of $SnCl_4$(g) produces radial growth of a $Ge_{0.906}Sn_{0.094}$ shell,[11] in this case performed at 275 °C. The planar thin film sample, on the other hand, was prepared by depositing a 330 nm $Ge_{0.895}Sn_{0.105}$ thin film on a 530 nm epitaxial Ge buffer layer deposited on a Si (100) substrate by molecular beam epitaxy (MBE), at a substrate temperature less than 150 °C to suppress the surface segregation of Sn. A detailed description of the MBE system and the Ge buffer growth method can be found elsewhere.[12] An x-ray diffraction (XRD) reciprocal space map (RSM) was used to evaluate the crystal quality, Sn content, and strain level of the GeSn film. The measured RSM is shown in Fig. 1(a) and demonstrates that the Ge buffer layer is strain relaxed, while the GeSn film is in a nearly pseudomorphic state of strain relative to the Ge buffer. The Sn content (x), in-plane strain ($\varepsilon_{\parallel}$), out-of-plane strain ($\varepsilon_{\perp}$), and strain relaxation (R) of the GeSn and Ge buffer layers are calculated and summarized in Table I. The strain relaxation (R) in the GeSn layer was calculated using the following relation:

$$R = \frac{a_{\parallel} - a_s}{a_r - a_s},$$

where $a_{\parallel}$ is the in-plane lattice constant and a_s is the lattice constant of the Si substrate. a_r is estimated using the equation $a_r = \frac{1-\nu}{1+\nu}a_{\perp} + \frac{\nu}{1+\nu}a_{\parallel}$, where $a_{\perp}$ is the out-of-plane lattice constant, and ν is the Poisson ratio following Vegard's law.[13] GeSn layer thickness and Sn composition were also validated by time-of-flight secondary ion mass spectrometry (ToF-SIMS) measurements. The SIMS profile is shown in Fig. 1(b). Both characterization methods give Sn compositions of about 10.5 at. %.

Single crystalline samples grown on bulk single crystal substrates, such as those used in this work, can be difficult samples for EXAFS for a number of reasons. First, in the grazing incidence geometry that is necessary for the measurements, data can be contaminated by the substrate's and film's Bragg peaks, which has been addressed by spinning the sample.[14] There is also the

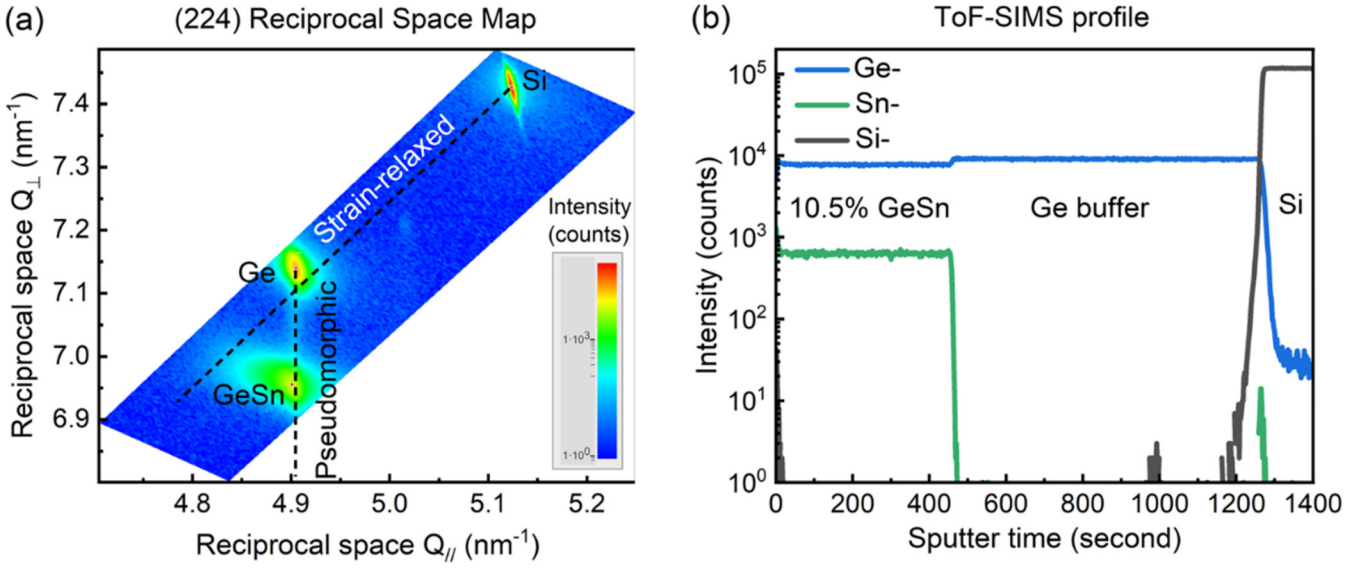

FIG. 1. (a) X-ray diffraction reciprocal space map near the (224) peak of the as-grown sample showing peaks from the Si substrate, strain relaxed Ge buffer, and pseudomorphic Ge–Sn film. (b) Secondary ion mass spectrometry plot of the as-grown sample showing Ge, Sn, and Si depth profiles.

© Author(s) 2025

Version of Record at:
https://doi.org/10.1063/5.0245736

TABLE I. Lattice constants (a_0), in-plane strain ($\varepsilon_{\parallel}$), out-of-plane strain ($\varepsilon_{\perp}$), and strain relaxation (R), and Sn concentration of the GeSn layer and the Ge buffer layer extracted from the XRD RSM.

Layer	a_0 (Å)	$\varepsilon_{\parallel}$(%)	$\varepsilon_{\perp}$(%)	R (%)	Sn (at. %)
Ge Buffer	5.6588	0.26	−0.19	106.4	0
GeSn	5.7456	−1.17	0.89	5.5	10.55

difficulty in this case that the Ge buffer is composed of an element that is also a component of the sample, meaning that any absorption by the Ge buffer will contribute erroneously to the data. Therefore, in this work, a process is employed to fabricate transferable GeSn microstructures (ribbons), which can be liberated from their growth substrate and are small enough to avoid self-absorption in fluorescence EXAFS. In order to fabricate such GeSn structures, patterning and a two-step etching process was used to form suspended GeSn ribbons.[15–17] A detailed description of the fabrication process can be found in the supplementary material, and the process flow is outlined in Fig. 2.[17] As shown in Fig. 2(a), the as-grown sample is first patterned to form ribbons, which are several μm wide and 10s of μm long, and a nonselective etch is used to etch through both Ge and GeSn. Next, a selective etch is used to etch Ge, thereby undercutting GeSn, as shown in Fig. 2(b), so that the ribbons can then be removed with a tape [Fig. 2(c)]. Liberation of GeSn from the growth substrate in this way avoids the difficulties associated with the presence of the substrate.

EXAFS data were collected at beamline 7–3[18] for the ribbons sample and beamline 11–2[19] for the nanowires sample at the Stanford Synchrotron Radiation Lightsource (SSRL) in fluorescence geometry with the sample loaded in a liquid He cryostat. In both cases, the sample consisted simply of the GeSn ribbons or nanowires held to the tape, which was used to remove them from the growth substrate. The Ge K-edge data were collected with a passivated implanted planar silicon (PIPS) detector, and the Sn K-edge data were collected with a 30-element monolithic Ge detector at 7–3 and a 100-element monolithic Ge detector at 11–2. In all cases, Soller slits and a filter were placed in front of the detectors to augment the signal-to-background ratio. A Ga filter was used for the Ge edge and a Cd filter for the Sn edge.

RESULTS AND DISCUSSION

Raw $\chi(k)$ data for both samples are shown in Fig. 3. It is immediately apparent that the datasets are quite similar. The main difference is the amplitude of the oscillations in the Sn edge data. This is, perhaps, even clearer in the absolute value of the Fourier

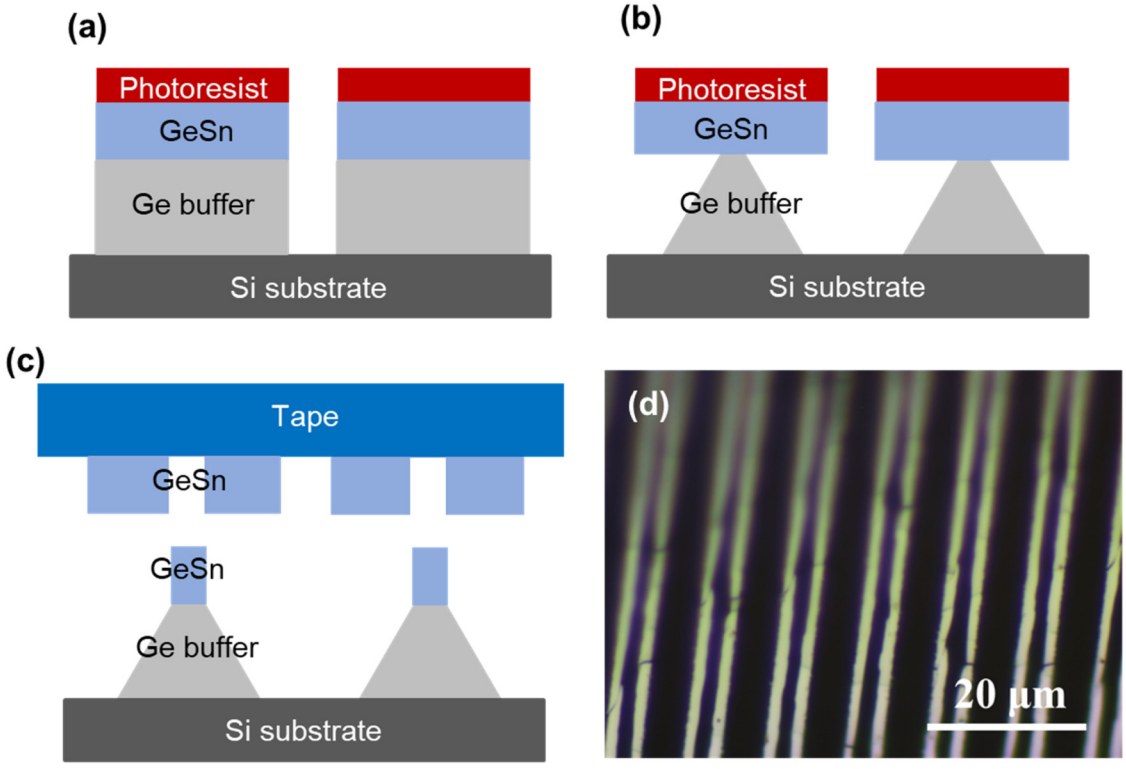

FIG. 2. Schematic process flow for the fabrication of the GeSn ribbon and removal from the substrate: (a) non-selective wet etching process with a Si substrate serving as the etch stop, (b) fabrication of suspended Ge–Sn microstructures on Ge by selective wet etching, (c) removal of the Ge–Sn ribbons with tape, and (d) optical microscope image showing that the removal of GeSn is as depicted in (c), with no Ge removed.

© Author(s) 2025

Version of Record at:
https://doi.org/10.1063/5.0245736

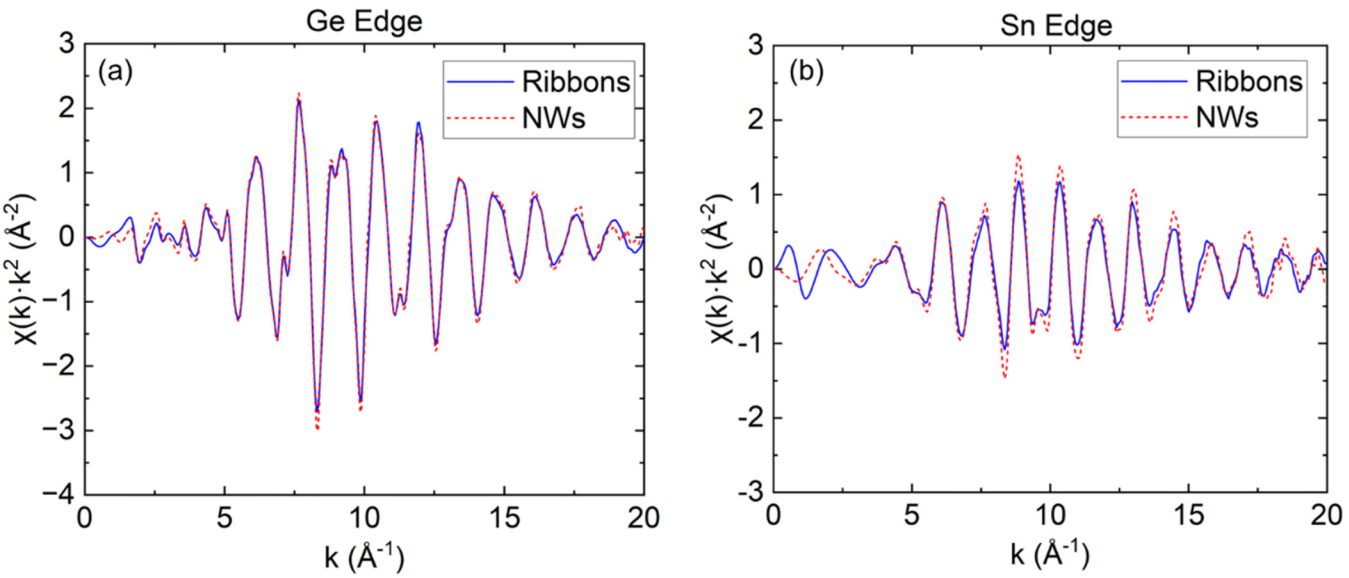

FIG. 3. Raw $\chi(k)$ data from both the MBE-GeSn ribbons sample (ribbons in legend), and Ge core/GeSn shell nanowires sample (NWs in legend): (a) Ge edge data and (b) Sn edge data.

transformations of the EXAFS shown in Fig. 4, where an overall decrease in the amplitude is seen for the ribbons, which were collected at BL 7–3, relative to the nanowires, which were collected at BLs 11–2. The decrease in the amplitude is further borne out by the fitted values of the amplitude reduction factor, which will be discussed below. It can likely be accounted for by the differences in the amplitude reduction factor at the two beamlines, given that both samples showed fitted values of the amplitude reduction

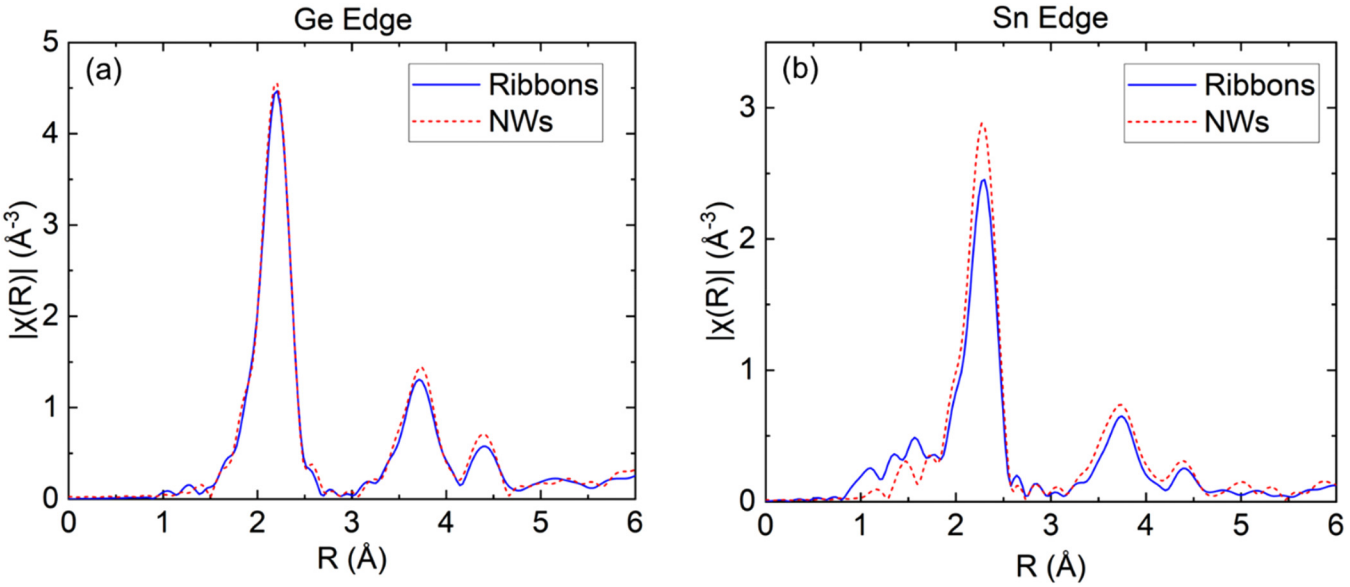

FIG. 4. Absolute value of the Fourier transform of the EXAFS, $|\chi(R)|$, for both the MBE-GeSn ribbons sample (ribbons in legend), and Ge core/GeSn shell nanowires sample (NWs in legend): (a) Ge edge data and (b) Sn edge data.

© Author(s) 2025

Version of Record at:
https://doi.org/10.1063/5.0245736

factors very similar to a Sn standard measured at each beamline (see the supplementary material).

Data analysis was performed using an approach similar to that described in our previous report.[8] The Sn edge data were averaged in SIXPACK[20] (reference to specific software packages and/or company names is made to adequately specify the methodology used and does not represent an endorsement by the National Institution of Standards and Technology, nor does it imply that the software or products identified are necessarily the best available for the purpose), which can handle data collected using the multi-element monolithic Ge detectors, while the Ge edge data were merged in Athena[21] (reference to specific software packages and/or company names is made to adequately specify the methodology used and does not represent an endorsement by the National Institution of Standards and Technology, nor does it imply that the software or products identified are necessarily the best available for the purpose) and further data reduction for both edges was also done in Athena[21] (reference to specific software packages and/or company names is made to adequately specify the methodology used and does not represent an endorsement by the National Institution of Standards and Technology, nor does it imply that the software or products identified are necessarily the best available for

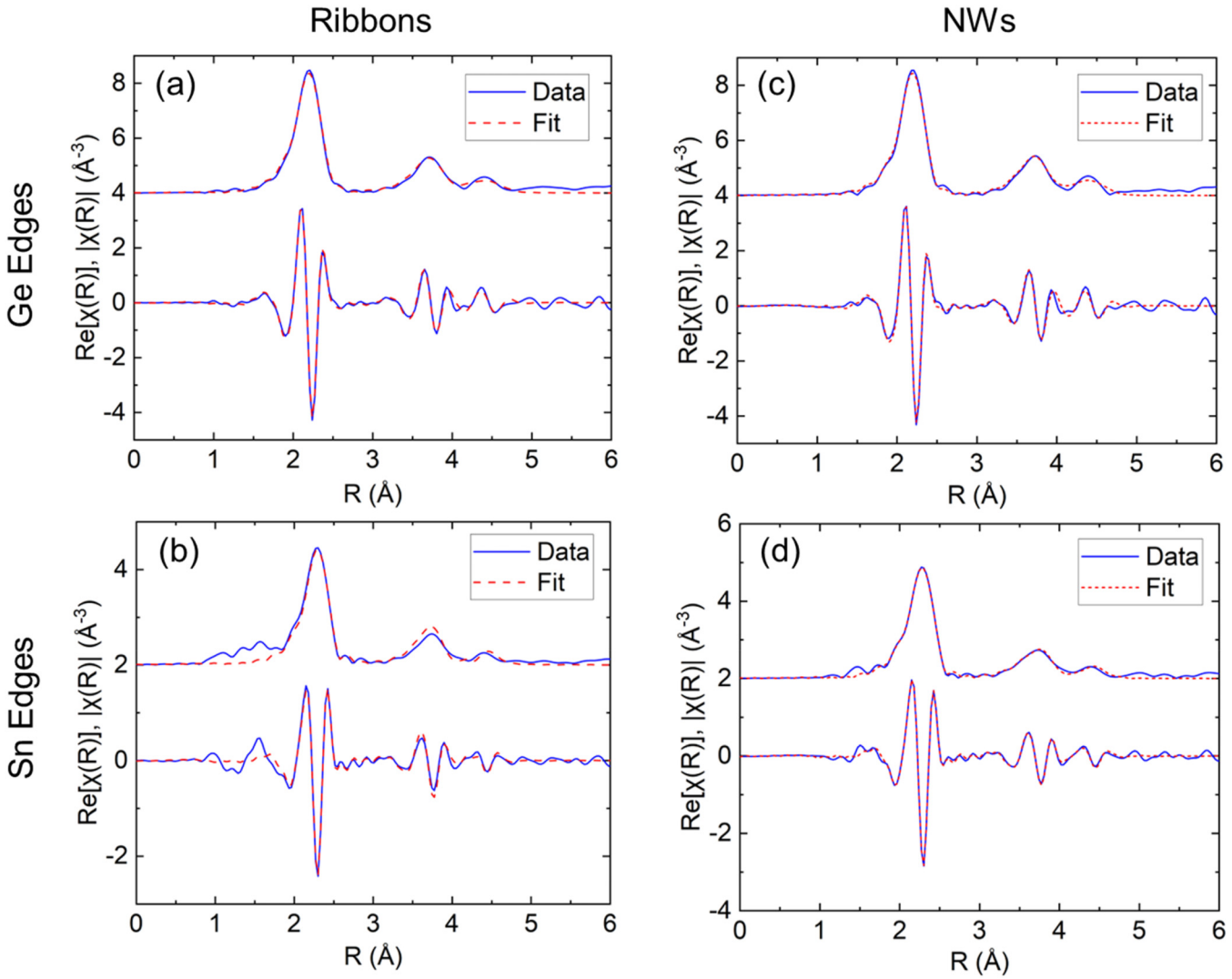

FIG. 5. EXAFS data and fits. In each panel, the top curves are the magnitude of the Fourier transform of the EXAFS, $|\chi(R)|$, and the bottom curves are the real part of the Fourier transform of the EXAFS, $Re(\chi(R))$, where R is the scattering path length. (a) Ge edge of the ribbons sample, (b) Sn edge of the ribbons sample, (c) Ge edge of the nanowires sample, and (d) Sn edge of the nanowires sample. [(c) and (d)] Reproduced with permission from Lentz *et al.*, Appl. Phys. Lett. **122**, 062103 (2023), Copyright 2023 AIP Publishing LLC.

© Author(s) 2025

Version of Record at:
https://doi.org/10.1063/5.0245736

TABLE II. Fitted values of the EXAFS fitting parameters for the two samples. Note that the initial values of interatomic distances (before fitting) are $R_1 = 2.45$ Å, $R_2 = 4.00$ Å, and $R_3 = 4.69$ Å, and the ΔR values below are reported relative to those initial values.

Parameter	Ribbons	Nanowires
S_0^2 Ge K-edge	0.99 ± 0.03	1.01 ± 0.05
S_0^2 Sn K-edge	0.79 ± 0.08	1.00 ± 0.06
ΔE_0 Ge K-edge (eV)	4.0 ± 0.6	3.8 ± 0.7
ΔE_0 Sn K-edge (eV)	6.7 ± 1.2	4.0 ± 0.8
ΔR_{1GeGe} (Å)	$4.8 \times 10^{-3} \pm 2 \times 10^{-3}$	$6.7 \times 10^{-3} \pm 2.5 \times 10^{-3}$
ΔR_{2GeGe} (Å)	$2.9 \times 10^{-2} \pm 5 \times 10^{-3}$	$2.4 \times 10^{-2} \pm 5 \times 10^{-3}$
ΔR_{3GeGe} (Å)	$5.4 \times 10^{-2} \pm 1 \times 10^{-2}$	$4.3 \times 10^{-2} \pm 1.1 \times 10^{-2}$
ΔR_{1GeSn} (Å)	$1.50 \times 10^{-1} \pm 4 \times 10^{-3}$	$1.45 \times 10^{-1} \pm 3 \times 10^{-3}$
ΔR_{2GeSn} (Å)	$9.1 \times 10^{-2} \pm 1.1 \times 10^{-2}$	$8.2 \times 10^{-2} \pm 7 \times 10^{-3}$
ΔR_{3GeSn} (Å)	$2.5 \times 10^{-2} \pm 2.8 \times 10^{-2}$	$3.8 \times 10^{-2} \pm 1.4 \times 10^{-2}$
ΔR_{1SnSn} (Å)	$2.9 \times 10^{-1} \pm 9 \times 10^{-2}$	$2.6 \times 10^{-1} \pm 2 \times 10^{-2}$
ΔR_{2SnSn} (Å)	$1.1 \times 10^{-1} \pm 3 \times 10^{-2}$	$1.7 \times 10^{-1} \pm 1 \times 10^{-2}$
ΔR_{3SnSn} (Å)	$-4.0 \times 10^{-2} \pm 3.2 \times 10^{-2}$	$-5.0 \times 10^{-2} \pm 2.2 \times 10^{-2}$
σ^2_{1GeGe} (Å^2)	$1.9 \times 10^{-3} \pm 2 \times 10^{-4}$	$1.9 \times 10^{-3} \pm 2 \times 10^{-4}$
σ^2_{2GeGe} (Å^2)	$6.9 \times 10^{-3} \pm 4 \times 10^{-4}$	$6.3 \times 10^{-3} \pm 4 \times 10^{-4}$
σ^2_{3GeGe} (Å^2)	$1.1 \times 10^{-2} \pm 1 \times 10^{-3}$	$9.4 \times 10^{-3} \pm 1.1 \times 10^{-3}$
σ^2_{1GeSn} (Å^2)	$1.7 \times 10^{-3} \pm 3 \times 10^{-4}$	$2.1 \times 10^{-3} \pm 2 \times 10^{-4}$
σ^2_{2GeSn} (Å^2)	$4.9 \times 10^{-3} \pm 1 \times 10^{-3}$	$8.0 \times 10^{-3} \pm 6 \times 10^{-4}$
σ^2_{3GeSn} (Å^2)	$1.1 \times 10^{-2} \pm 4 \times 10^{-3}$	$1.2 \times 10^{-2} \pm 2 \times 10^{-3}$
σ^2_{1SnSn} (Å^2)	$9 \times 10^{-3} \pm 1.2 \times 10^{-2}$	$4.0 \times 10^{-3} \pm 2.1 \times 10^{-3}$
σ^2_{2SnSn} (Å^2)	$2.6 \times 10^{-3} \pm 2 \times 10^{-3}$	$3.0 \times 10^{-3} \pm 9 \times 10^{-4}$
σ^2_{3SnSn} (Å^2)	$2.7 \times 10^{-3} \pm 2 \times 10^{-3}$	$3.8 \times 10^{-3} \pm 1.4 \times 10^{-3}$
x	0.12 ± 0.02	0.11 ± 0.02

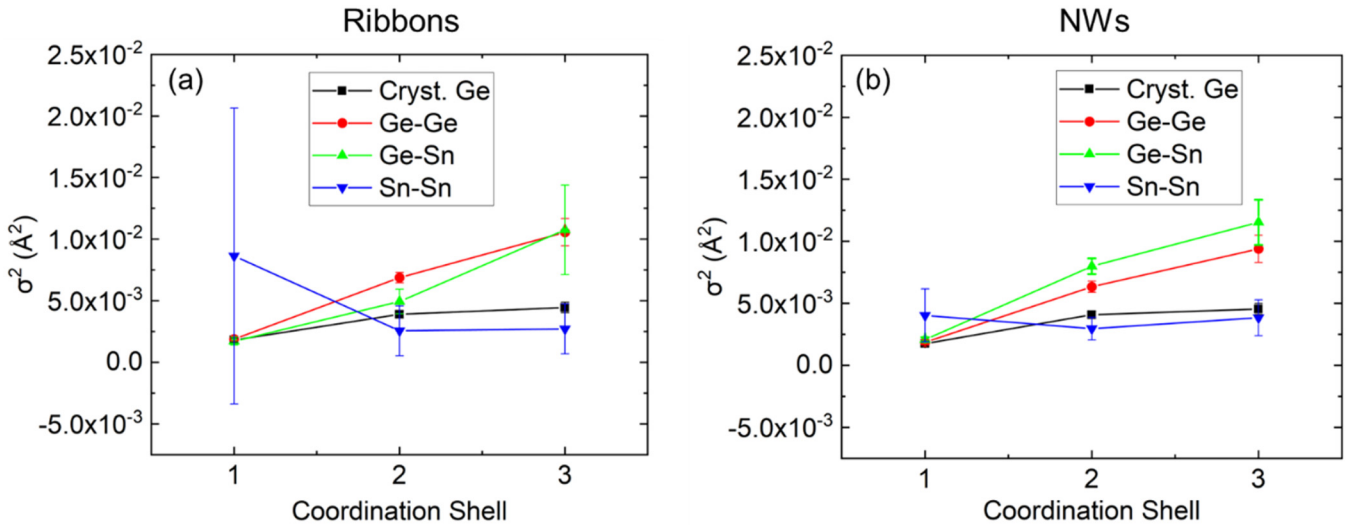

FIG. 6. MSRD for each path in (a) the ribbons sample and (b) the NW samples; each plot also includes the same reference pure crystalline Ge sample. For the paths labeled Ge–Ge and Sn–Sn, the first element in the legend is the absorber and the second is the scatterer, and for the path labeled Ge–Sn, paths with Ge absorption and Sn scatter are the same as those with Sn absorption and Ge scatter (*vide infra*).

© Author(s) 2025

Version of Record at:
https://doi.org/10.1063/5.0245736

the purpose). In the case of the data from the ribbons sample, the raw $\chi(k)$ data were Fourier transformed using a Hanning window with $dk = 1$ in the range of 3.0–19.7 Å^{-1} for both edges. A simultaneous fit to both edges was performed in R-space using Artemis[21] (reference to specific software packages and/or company names is made to adequately specify the methodology used and does not represent an endorsement by the National Institution of Standards and Technology, nor does it imply that the software or products identified are necessarily the best available for the purpose) and including k^2-weighted Ge data in the range 1.5–4.7 Å and Sn data in the range 1.8–4.7 Å. As in a previous report,[8] we adopt the approach of a simple fit composed of nine distinct single scattering paths: for Ge absorption, scatter from the first, second, and third nearest neighbor shells from either Sn or Ge (six paths); and for Sn

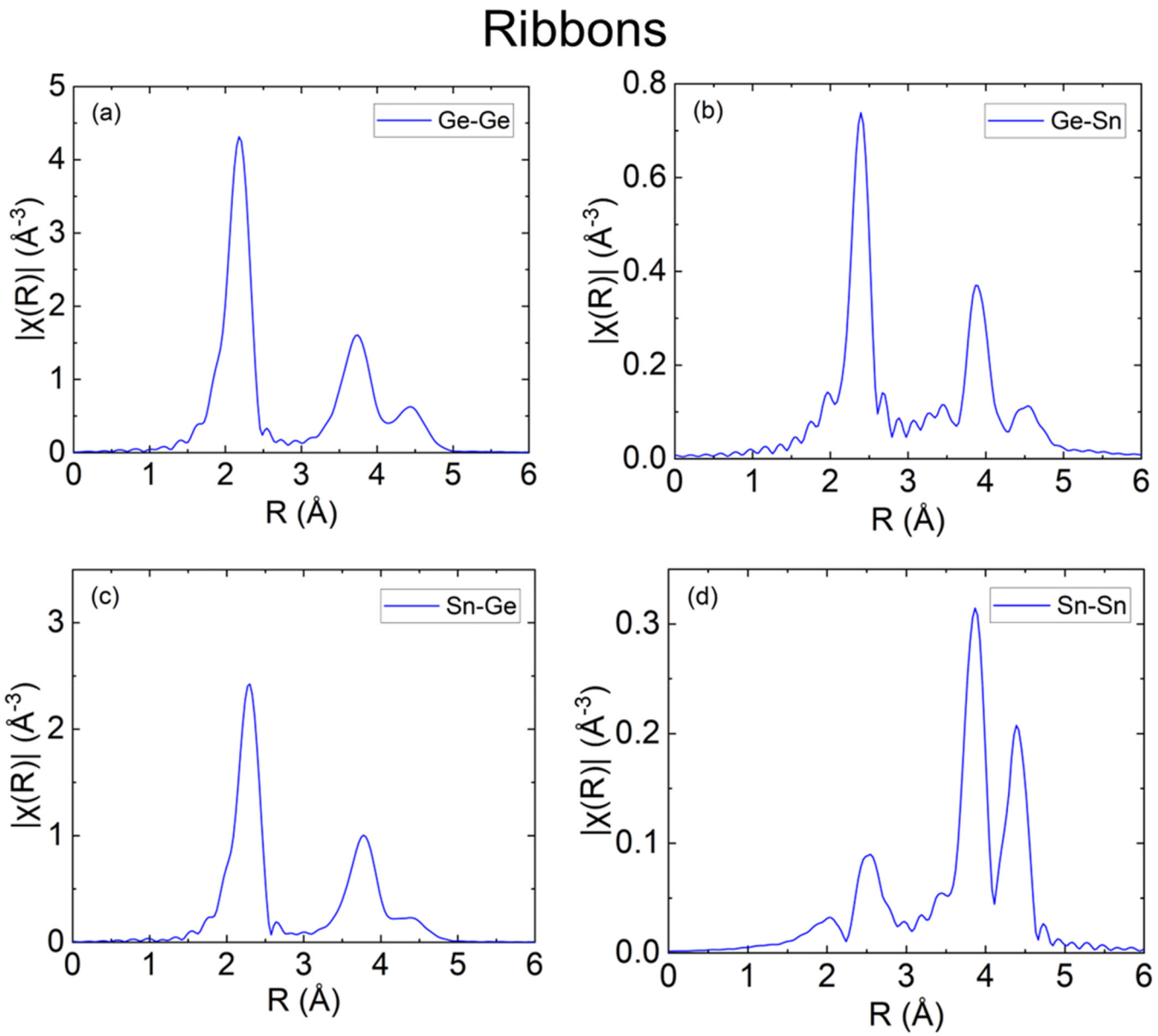

FIG. 7. Chemically specific single scattering paths in the ribbons sample. That is, each panel is the sum of the 1NN, 2NN, and 3NN fitted paths for a specific type of path, that is the chemical identity of the absorber and the scatterer in the path, (a) Ge–Ge paths, (b) Ge–Sn paths, (c) Sn–Ge paths, and (d) Sn–Sn paths. The first element in the legend is the scatterer, and the second is the absorber.

© Author(s) 2025

Version of Record at:
https://doi.org/10.1063/5.0245736

absorption, scatter from the first, second, and third nearest neighbor shells from either Sn or Ge (three new paths, as paths with Sn absorption and Ge scatter and paths with Ge absorption and Sn scatter were taken to have equivalent parameters in the fit). The composition was included and fit by incorporating a factor x, representing Sn mol fraction, in the amplitude for paths with Sn scatter and $1 - x$ for paths with Ge scatter. The fit, therefore, contained a total of 23 variables: the amplitude reduction factor for Ge and Sn edges, the energy shift for Ge and Sn edges, nine changes in path length, and nine mean squared relative displacements (MSRD) (σ^2), one for each path, and Sn mol fraction x. The data and fits for both the Ge and Sn edges for both samples are shown in Fig. 5. The fits closely follow the data.

The fitted values of all parameters are shown in Table II. The values of the MSRD warrant further discussion. The fitted values of the MSRD parameters for both samples are shown in Fig. 6. All

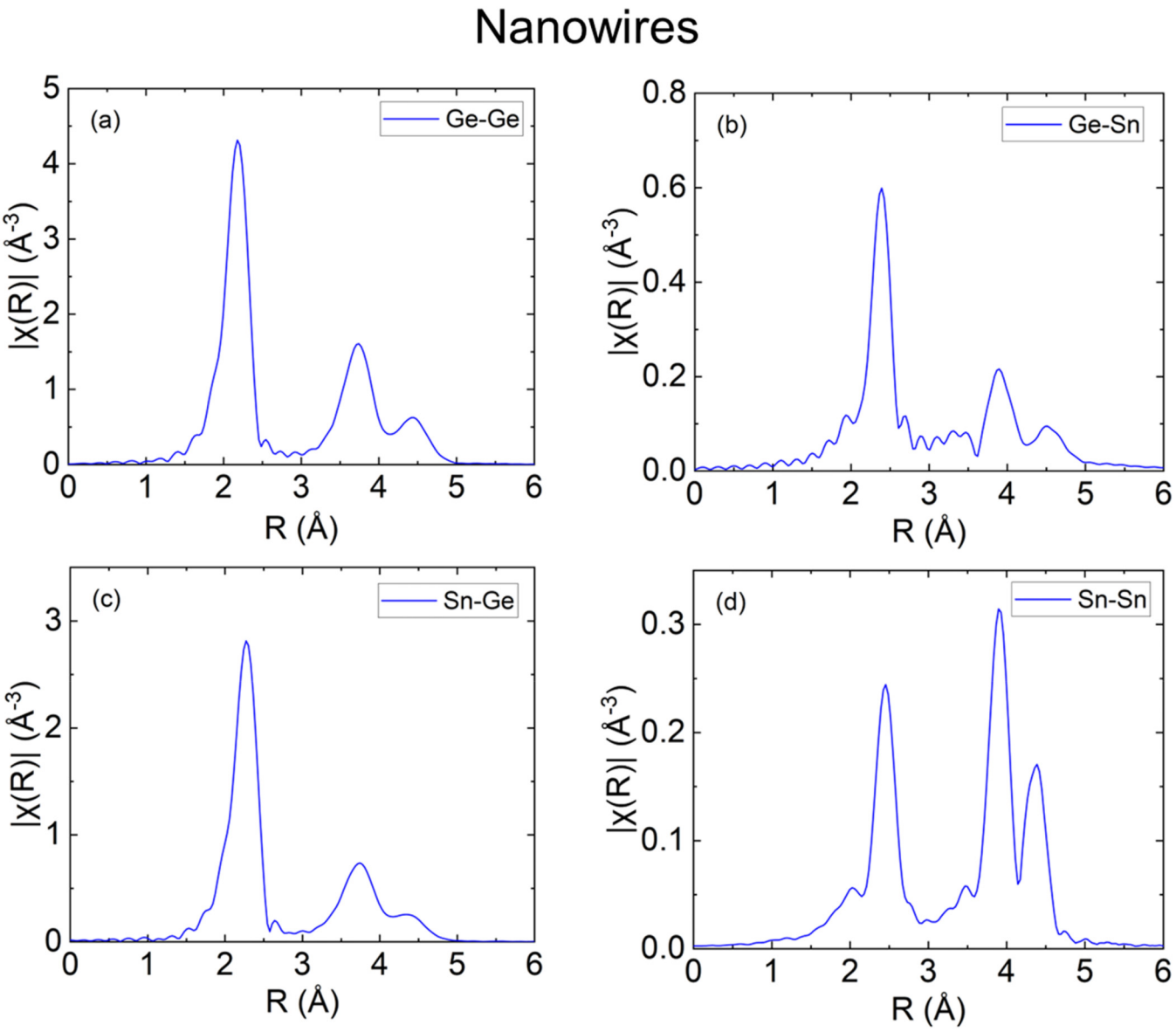

FIG. 8. Chemically specific single scattering paths in the NW sample. That is, each panel is the sum of the 1NN, 2NN, and 3NN fitted paths for a specific type of path, that is the chemical identity of the absorber and the scatterer in the path, (a) Ge–Ge paths, (b) Ge–Sn paths, (c) Sn–Ge paths, and (d) Sn–Sn paths. The first element in the legend is the scatterer, and the second is the absorber. Reproduced with permission from Lentz *et al.*, Appl. Phys. Lett. **122**, 062103 (2023), Copyright 2023 AIP Publishing LLC.

© Author(s) 2025

Version of Record at:
https://doi.org/10.1063/5.0245736

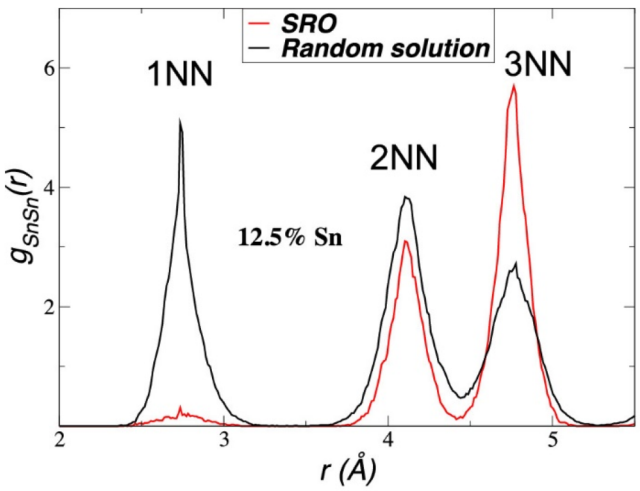

FIG. 9. Calculated Sn–Sn radial distribution function for a GeSn alloy with 12.5% Sn in both the random alloy and more-favorable short-range order cases. Reproduced with permission from Cao *et al.*, ACS Appl. Mater. Interfaces **12**, 57245 (2020), Copyright 2020 American Chemical Society.

paths *with the notable exception of the Sn–Sn paths* closely follow the well-established trend of increasing MSRD with increasing shell.[22] In addition, it is evident that the MSRD value for the path with Sn absorption and scatter from a 1NN Sn atom is even more anomalous when compared to the other three first neighbor paths for both samples, and even more so for the MBE-grown GeSn ribbons sample than for the nanowires. Its value is considerably much too large and is coupled with extremely large uncertainty.

As demonstrated previously,[8] insight into the MSRD values can be gained from the chemically specific sums of paths, which are shown in Fig. 7 for the ribbons sample. Clearly, the amplitude of the Sn–Sn 1NN path is greatly suppressed compared to the other 1NN paths. This leads to the conclusion that similar to the findings of Ref. 8 and as predicted theoretically,[1] the MBE-grown GeSn film shows a significant SRO such that the Sn atoms repel the neighboring Sn atoms. This can be understood by considering that the observed intensity of an EXAFS oscillation is proportional to the product of the coordination number and the $\exp(-2\sigma^2 * k^2)$ of that path with the coordination number and the MSRD consequently being highly correlated parameters in an EXAFS fit. This high correlation means that in an EXAFS fit, purely from a mathematical perspective, increasing the value of the MSRD increases the value of the coordination number and vice versa. These results, therefore, suggest that this SRO phenomenon is typical of the GeSn system and not confined to relatively strain-free nanowire shells. In fact, it seems that the SRO is stronger in these films than in the nanowire shells, as the amplitude of the 1NN Sn–Sn path is significantly smaller relative to the 2NN and 3NN paths in the ribbons than in the NWs (cf. Figs. 7 and 8). This observation is consistent with the fact that we could not quantitatively deduce the reduction in Sn–Sn nearest neighbors in the ribbons by the introduction of the previously employed swap parameter in the fit and the much larger error bars of its MSRD.[8]

It has been predicted that Sn atoms rejected from the first shell around other Sn atoms in GeSn should primarily populate the third shell, as shown in Fig. 9, reproduced from Ref. 1. This is also

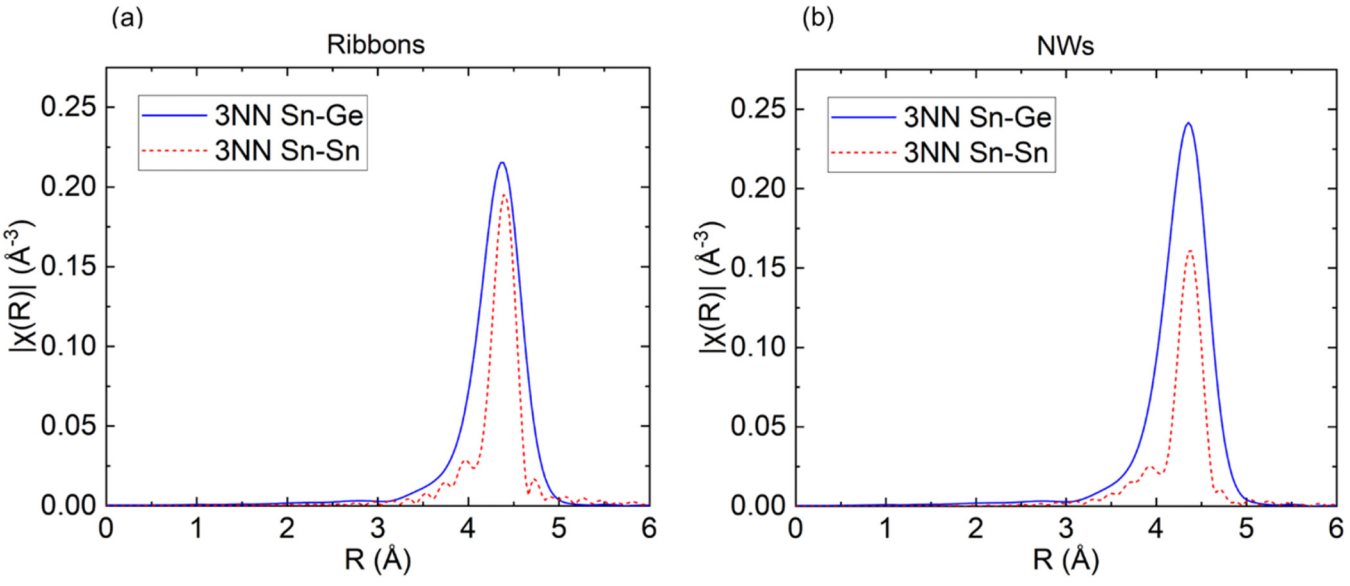

FIG. 10. Fitted third nearest neighbor paths in the Sn edge data of (a) the ribbons sample and (b) the NW sample. The first element in the legend is the absorber and second is the scatterer.

© Author(s) 2025

Version of Record at:
https://doi.org/10.1063/5.0245736

consistent with the MSRD values in Fig. 6. It is generally the case that longer paths have larger MSRD values than shorter ones, because atomic vibrations are less correlated when the atoms involved are further apart.[23] In this case, our EXAFS data of very high statistical quality show that the longer Sn–Sn paths have **much lower** MSRD than do the longer Ge–Sn or Ge–Ge paths. This is highly suggestive of increased Sn–Sn coordination in these shells on account of the correlation between coordination and MSRD explained above.

We may gain further clarification by examining the fitted third shell paths in the Sn edge data from the two samples. These paths are plotted in Fig. 10 and reveal a larger Sn–Sn intensity relative to the Sn–Ge intensity in the ribbons sample than in the nanowires sample. Under the assumption that the actual MSRD for these paths should not vary from sample to sample, the sample dependent relative intensities of these paths suggest an increase in the Sn content in the third shell (viewed from an Sn atom) in the ribbons vs the nanowires sample.

To summarize, given the detection of the SRO in Ge–Sn in our previous report,[8] as well as the theoretical prediction thereof,[1] the instability in the fit when incorporating the swap parameter, and relative amplitudes of the 3NN paths between the two samples, it seems most likely that the 1NN Sn–Sn path is less significant in the ribbons sample due to a stronger SRO in this MBE-grown GeSn planar film compared to the CVD-grown Ge core/GeSn nanowires measured previously. Although these effects are difficult to quantify, the behavior observed in the EXAFS data appears to be in good agreement with theoretical predictions.

SRO may be stronger in the MBE films when compared to the nanowires for several reasons. If the SRO, in which Sn–Sn nearest neighbors are far rarer than in a random alloy, is, indeed, the favorable configuration for GeSn, as has been predicted,[1] one might expect a dependence of the observed SRO on the crystal growth rate, with lower rates favoring a greater SRO.[24–26] As it happens, the GeSn growth rates in the MBE and CVD processes studied are similar. The GeSn nanowire shells grow at an average rate of ~1 nm/min (decreasing with increasing shell thickness), whereas the MBE-grown GeSn film grows at ~0.8 nm/min. Additionally, in MBE growth, pure atomic species (Ge and Sn) are incident on the sample, whereas in CVD, a relatively complex gas phase and surface chemistry are involved. It is possible that simultaneous etching during growth and the presence of surface adsorbates during CVD may affect the extent to which the SRO develops.

A possibly significant difference is that, in nanowire shell growth, a GeSn film can be essentially free of residual strains arising from lattice mismatch with the Ge core for the growth of sufficient shell thickness.[10] The MBE-GeSn films grown on bulk substrates with a relaxed Ge buffer layer exhibit a large biaxial compressive strain (Table I). This may increase the driving force for the nearest neighbor Sn atom repulsion, relative to an unstrained film. If so, biaxial strain in the MBE-grown GeSn may result in a greater SRO if there is sufficient Sn atom mobility for rearrangement to occur after the Sn atoms incorporate in the crystal. Moreover, the GeSn shells grow on (112) nanowire sidewall surface facets and (110) vertices, rather than the (100)-oriented surface habit of the MBE films studied herein. The growth of GeSn alloys on (112) vs (110) facets has been shown to affect local Sn incorporation.[10,27] It may also affect the SRO relative to (100) growth.

The 3NN Sn–Sn path in the ribbons sample also reveals a long-range structural disorder in the film. Such higher shell disorder is likely present due to an inhomogeneous strain and the presence of threading dislocations incorporated in the as-grown MBE-GeSn epitaxial films. The presence of threading (and misfit) dislocations in the MBE-GeSn epilayer occurs because of its growth on a relaxed Ge virtual substrate. The process of cyclic thermal annealing that leads to a relaxed Ge virtual substrate on Si, a common approach for producing a template for GeSn growth on Si, produces a network of dislocations that propagate into the overlying GeSn film.[28] Such defects present in the GeSn ribbons would likely increase the MSRD measured in EXAFS[29] together with an increased MSRD because of the bond-length disorder produced by the strain itself.[30,31]

To directly witness the long-range increase in structural disorder in the 3NN shell, Fig. 11 shows the back transform of the Ge *K*-edge EXAFS data from the two samples performed for R = 4.1–4.7 Å. The amplitude of the 3NN shell is suppressed in the ribbons when compared to the nanowires, especially at higher wavenumbers, indicative of an increased long-range MSRD in the nanowires sample.

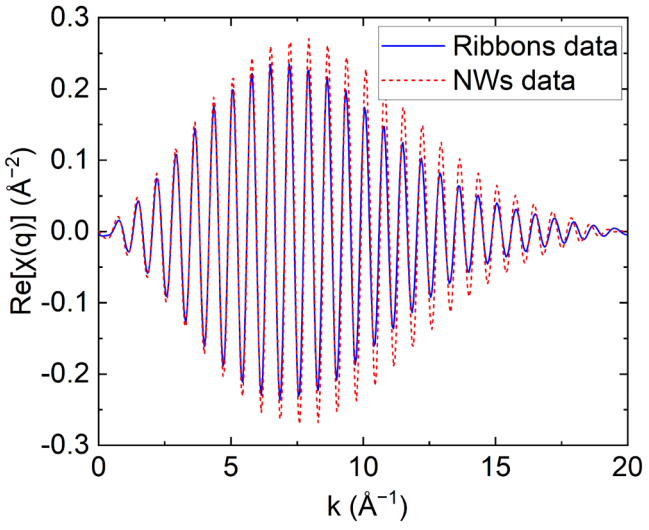

FIG. 11. Back transforms of the 3NN shell for the Ge edge data for both the GeSn ribbons sample and the Ge core/GeSn shell nanowires sample.

CONCLUSIONS

In this work, EXAFS was used to probe local atomic positions in a GeSn alloy thin film grown by molecular beam epitaxy on an epitaxial Ge buffer layer itself grown on a Si (100) substrate. A novel preparation technique using patterning and undercut etching of the GeSn epilayer was used to prepare samples for EXAFS measurements. In comparison with the previously reported short-range order in GeSn shells grown epitaxially around misfitting Ge nanowire cores by chemical vapor deposition, the EXAFS analysis of the MBE-grown ribbons is consistent with an even greater degree

© Author(s) 2025

Version of Record at:
https://doi.org/10.1063/5.0245736

of short-range order, characterized by a greatly reduced coordination of the Sn atoms by the first nearest neighbor Sn compared to a random alloy. The analysis of the mean squared relative displacement values for atoms along different scattering paths extracted from fits to the EXAFS data suggests that Sn atoms have greater coordination in Sn third nearest neighbor sites, and this effect is more pronounced in the MBE-grown films than in the CVD-grown GeSn shells. These results suggest that the development of SRO is a common phenomenon in GeSn alloys, and its extent depends on the growth-related factors that require further elucidation. Finally, the EXAFS measurements also revealed increased disorder in the ribbons sample at a longer range, consistent with strain-induced bond distortion and dislocations that propagate into them from the Ge buffer layer during GeSn MBE growth.

SUPPLEMENTARY MATERIAL

See the supplemental material for the description of the GeSn ribbon fabrication process, EXAFS data and fits from the Sn standard at each beamline, and the EXAFS fitting procedure.

ACKNOWLEDGMENTS

This research was supported by the U.S. National Science Foundation under Grant No. DMR-2003266. This funding primarily supported growth of the nanowires sample. This research was supported by the U.S. Department of Energy under Award No. DE-SC0023412 and Subaward No. UA2023-351. This funding primarily supported EXAFS characterization. The use of the Stanford Synchrotron Radiation Lightsource, SLAC National Accelerator Laboratory, was supported by the U.S. Department of Energy, Office of Science, Office of Basic Energy Sciences under Contract No. DE-AC02-76SF00515. Part of this work was performed at the Stanford Nano Shared Facilities (SNSF), supported by the National Science Foundation under Award No. ECCS-2026822. This research was supported by the U.S. National Science Foundation, NSF Fuse Program, Grant No. 2328840. This funding primarily supported MBE growth and sample preparation. Additional support was provided by the National Institute of Standards and Technology.

AUTHOR DECLARATIONS

Conflict of Interest

The authors have no conflicts to disclose.

Author Contributions

J. Zachary Lentz: Conceptualization (equal); Data curation (lead); Formal analysis (lead); Investigation (lead); Methodology (lead); Visualization (lead); Writing – original draft (lead); Writing – review & editing (lead). **Haochen Zhao:** Data curation (supporting); Formal analysis (supporting); Investigation (supporting); Validation (supporting); Visualization (supporting); Writing – original draft (supporting); Writing – review & editing (supporting). **J. C. Woicik:** Formal analysis (supporting); Investigation (supporting); Methodology (supporting); Validation (supporting); Writing – review & editing (supporting). **Yuping Zeng:** Funding acquisition (supporting); Project administration (supporting); Resources (supporting); Supervision (supporting); Validation (supporting); Writing – review & editing (supporting). **Paul C. McIntyre:** Conceptualization (lead); Funding acquisition (lead); Methodology (lead); Project administration (lead); Resources (lead); Supervision (lead); Validation (lead); Writing – original draft (supporting); Writing – review & editing (supporting).

DATA AVAILABILITY

The data that support the findings of this study are available from the corresponding author upon reasonable request.

REFERENCES

[1]B. Cao, S. Chen, X. Jin, J. Liu, and T. Li, ACS Appl. Mater. Interfaces **12**, 57245 (2020).
[2]S. Chen, X. Jin, W. Zhao, and T. Li, Phys. Rev. Mater. **8**, 43805 (2024).
[3]X. Jin, S. Chen, and T. Li, Commun. Mater. **3**, 66 (2022).
[4]X. Jin, S. Chen, C. Lemkan, and T. Li, Phys. Rev. Mater. **7**, L111601 (2023).
[5]S. Mukherjee, N. Kodali, D. Isheim, S. Wirths, J. M. Hartmann, D. Buca, D. N. Seidman, and O. Moutanabbir, Phys. Rev. B **95**, 161402(R) (2017).
[6]S. Assali, J. Nicolas, S. Mukherjee, A. Dijkstra, and O. Moutanabbir, Appl. Phys. Lett. **112**, 251903 (2018).
[7]S. Liu, A. C. Covian, X. Wang, C. T. Cline, A. Akey, W. Dong, S.-Q. Yu, and J. Liu, Small Methods **6**, 2200029 (2022).
[8]J. Z. Lentz, J. C. Woicik, M. Bergschneider, R. Davis, A. Mehta, K. Cho, and P. C. McIntyre, Appl. Phys. Lett. **122**, 062103 (2023).
[9]Y. Wang, A. C. Meng, P. C. McIntyre, and W. Cai, Nanoscale **11**, 21974 (2019).
[10]A. C. Meng *et al.*, Mater. Today Nano **5**, 100026 (2019).
[11]A. C. Meng, C. S. Fenrich, M. R. Braun, J. P. McVittie, A. F. Marshall, J. S. Harris, and P. C. McIntyre, Nano Lett. **16**, 7521 (2016).
[12]H. Zhao, G. Lin, C. Han, R. Hickey, T. Zhama, P. Cui, T. Deroy, X. Feng, C. Ni, and Y. Zeng, Vacuum **210**, 111868 (2023).
[13]L. Vegard, Z. Phys. **5**, 17 (1921).
[14]J. Woicik and K. Miyano, Phys. Rev. B **57**, 14592 (1998).
[15]G. Lin, P. Cui, T. Wang, R. Hickey, J. Zhang, H. Zhao, J. Kolodzey, and Y. Zeng, IEEE Trans. Nanotechnol. **20**, 846 (2021).
[16]Y. Han, Y. Li, Y. Song, C. Chi, Z. Zhang, J. Liu, Z. Zhu, and S. Wang, Semicond. Sci. Technol. **33**, 085011 (2018).
[17]H. Zhao *et al.*, J. Vac. Sci. Technol., B **42**, 042205 (2024).
[18]See https://www-ssrl.slac.stanford.edu/content/beam-lines/bl7-3 for information on the specifications of beamline 7-3 at SSRL.
[19]See https://www-ssrl.slac.stanford.edu/content/beam-lines/bl11-2 for information on the specifications of beamline 11-2 at SSRL.
[20]S. M. Webb, Phys. Scr. **115**, 1011 (2005).
[21]B. Ravel and M. Newville, J. Synchrotron Radiat. **12**, 537 (2005).
[22]A. Di Cicco, N. V. Pavel, A. Bianconi, A. Benfatto, and C. R. Natoli, J. Phys. C **8**, 71 (1986).
[23]A. Frenkel, E. A. Stern, A. Voronel, A. Qian, and M. Newville, Phys. Rev. B **49**, 11662 (1994).
[24]E. Antillon, C. Woodward, S. I. Rao, B. Akdim, and T. A. Parthasarathy, Acta Mater. **190**, 29 (2020).
[25]D. de Fontaine, "Clustering effects in solid solutions," in *Treatise on Solid State Chemistry: Changes of State* (Springer, 1975), Vol. 5, pp. 129–178.
[26]F. Otto, A. Dlouhý, C. Somsen, H. Bei, G. Eggeler, and E. P. George, Acta Mater. **61**, 5743 (2013).
[27]S. Assali *et al.*, ACS Nano **14**, 2445 (2020).
[28]A. Mosleh *et al.*, ECS Trans. **64**, 895 (2014).
[29]D. R. Black, J. C. Woicik, M. Erdtmann, and T. A. Langdo, Appl. Phys. Lett. **88**, 0224102 (2006).
[30]J. Woicik, C. Bouldin, and K. Miyano, Phys. Rev. B **55**, 15386 (1997).
[31]J. C. Woicik, Surf. Sci. Rep. **69**, 38 (2014).

© Author(s) 2025